Journal of Materials Chemistry A

ROYAL SOCIETY OF CHEMISTRY

PAPER

View Article Online
View Journal | View Issue

Open Access Article. Published on 11 December 2023. Downloaded on 11/9/2025 9:25:01 AM. This article is licensed under a Creative Commons Attribution 3.0 Unported Licence.

Check for updates

Cite this: J. Mater. Chem. A, 2024, 12, 1779

Subnanometric Pt clusters dispersed over Cs-doped TiO_2 for CO_2 upgrading *via* low-temperature RWGS: *operando* mechanistic insights to guide an optimal catalyst design†

Guillermo Torres-Sempere,[a] Rubén Blay-Roger,[a] Ligia A. Luque-Álvarez,[a] José L. Santos,[ab] Luis F. Bobadilla,[a] Laura Pastor-Pérez,[a] Miguel A. Centeno,[a] Willinton Y. Hernández,[c] Ibraheem Yousef,[c] José A. Odriozola[a] and Tomas R. Reina*[a]

The RWGS reaction is gathering momentum as an effective route for CO_2 valorisation and given its endothermic nature the challenge lies in the design of active low-temperature catalysts. Herein we have designed two catalysts based on subnanometric Pt clusters providing effective CO_2 conversion and, more importantly, high CO selectivity in the low-temperature range. The impact of Cs as a dopant in the catalyst's formulation is crucial leading to full selectivity at 300 °C. The reaction mechanisms for the studied systems namely Pt/TiO_2 and PtCs/TiO_2 are significantly different due to the presence of the alkali promoter. The presence of Cs neutralises the hydroxide groups of the TiO_2 surface, changing the reaction pathway. The Pt/TiO_2 catalyst follows a redox mechanism where CO_2 dissociates to CO in the oxygen vacancies, and then these vacancies are recovered by the migration of H_2 by spill over phenomena. On the other hand, the Cs doped catalyst has two possible mechanism pathways: the (ii) formyl/acyl pathway, where –CHO species are formed and, depending on the reaction conditions, evolve to CO gas or oxygenated compounds, and (ii) frustrated Lewis pair (FLP) assisted CO_2 reduction route, in which the FLP induces the heterolytic dissociation of H_2 and the subsequent hydrogenation of CO_2 to CO. The latter route enabled by Cs-doping combined with the subnanometric Pt domains seems to be responsible for the excellent catalytic behaviour leading to fully selective low-temperature RWGS systems and thus unlocking new possibilities for less energy demanding CO_2 valorisation units based on RWGS.

Received 8th September 2023
Accepted 7th December 2023

DOI: 10.1039/d3ta05482a

rsc.li/materials-a

1. Introduction

The extensive use of fossil fuels such as coal or natural gas is promoting the increase of carbon dioxide in our atmosphere, reaching historical concentration values of 411 ppm.[1] There is much debate within the scientific community on how to address this pressing problem and among the alternatives, chemical CO_2 recycling by its transformation into added value products is a preferred strategy.[2] One of the most interesting ways of accomplishing this upgrading is CO_2 hydrogenation, aiming at the production of long-chain hydrocarbons or methanol, among other highly valuable chemicals and fuels.[3] Within the different possibilities, the RWGS reaction (eqn (1)) stands out as a direct route for gas-phase CO_2 upgrading:[4]

$$CO_2 + H_2 \leftrightharpoons CO + H_2O,\ \Delta H_{298K} = 41.2\ \text{kJ mol}^{-1} \quad (1)$$

Indeed the RWGS yields syngas, which is an extraordinary and valuable platform for chemical and fuel synthesis at the industrial level.[5] Furthermore, this reaction can use atmospheric CO_2 through direct air-capture conversion schemes or CO_2 emitted from industrial flue gases, reducing its concentration and contributing to a circular economy.[6] In any case the successful implementation of the RWGS technology is intimately linked to green hydrogen availability, and in this sense our recent techno-economic assessment validates the RWGS route.[7]

The main drawback of RWGS is its endothermic nature, requiring high temperatures to achieve CO_2 equilibrium conversions ranging between 10% and 50% at 200–500 °C, respectively, which entails high energy consumption and limits

[a]Inorganic Chemistry Department and Materials Sciences Institute, University of Seville-CSIC, Sevilla, 41092, Spain. E-mail: tramirez@us.es
[b]King Abdullah University of Science and Technology, Thuwal, Saudi Arabia
[c]Alba Synchrotron, Carrer de la Llum 2-26, Cerdanyola del Vallès, 08290, Barcelona, Spain

† Electronic supplementary information (ESI) available. See DOI: https://doi.org/10.1039/d3ta05482a

Open Access Article. Published on 11 December 2023. Downloaded on 11/9/2025 9:25:01 AM.
This article is licensed under a Creative Commons Attribution 3.0 Unported Licence.

its commercial application.[8] Furthermore, CO_2 is a stable molecule, so active catalysts are needed for this process. Hence the challenge for the catalysis community can simply be formulated as follows: is there a way to design effective low-temperature RWGS catalysts? Well, here the major bottleneck is the reaction selectivity in the low-temperature operational window. Indeed, at low temperature, competitive processes such as the forward water–gas shift reaction (eqn (2)) and CO_2 methanation (eqn (3)) are favoured:[9]

$$CO + H_2O \leftrightharpoons CO_2 + H_2,\ \Delta H_{298K} = -41.2\ \text{kJ mol}^{-1} \quad (2)$$

$$CO_2 + 4H_2 \leftrightharpoons CH_4 + 2H_2O,\ \Delta H_{298K} = -165\ \text{kJ mol}^{-1} \quad (3)$$

Current catalytic formulations for RWGS have failed to overcome the low-temperature limitation. For instance, noble metals such as Au,[10] Pt,[11] Pd[12] or Rh[13] and non-noble metals (Cu,[14] Fe[15] or Cr[16]) as the active phases over diverse oxidic supports (Al_2O_3, TiO_2, SiO_2, ZrO_2 and CeO_2)[17–22] have been studied with successful results mainly at temperatures beyond 500 °C. Among these catalysts, Pt/TiO_2 has shown interesting catalytic activity, specifically when small Pt particle size and high dispersion are achieved and when TiO_2 morphology and its reducibility are optimised. In fact, Pt and TiO_2 can present strong metal–support interaction (SMSI), which can produce reduction sites on the TiO_2 surface.[23,24] Furthermore, the application of Pt atomically dispersed on reducible metal oxides for RWGS exhibits an excellent opportunity to maximize the atom-utilization efficiency with well-defined single active sites and increase specific product selectivity. For instance, Zhao *et al.*[11] found that atomically dispersed Pt species showed weak adsorption strength toward CO preventing subsequent hydrogenation into methane and promoting CO selectivity in RWGS. On the other hand, the role of promoters is deemed fundamental to suppress the competitive reactions and favour RWGS at low temperatures. Among the different reported promoters that can be used in RWGS catalysts, Cs is deemed promising in terms of selectivity and activity enhancement. This is ascribed to its large ionic radius and very low ionization potential energy, which can help in the activation and reduction of CO_2.[25,26]

Beyond catalyst selection, the design of highly efficient RWGS catalysts requires the integration of spectroscopic and microscopic tools allowing for the design and synthesis of new materials with structural and chemical properties that are well defined. This can only be achieved with the use of complex and sophisticated techniques allowing the study of the catalyst, the gas phase and the adsorbed intermediates under the actual reaction conditions. A deep understanding of the reaction mechanism may help to improve the global process and to design optimal catalytic materials. Although the reaction mechanism is still a subject for debate, two principal pathways have been suggested to govern the RWGS reaction: the regenerative redox mechanism and the associative one.[27] In the redox mechanism, hydrogen simply plays a role as a reducing agent without participating in the formation of intermediates. Usually, in this mechanistic route, the support presents redox properties. Therefore, the whole process would consist of the reduction of the support by the H_2 and the reoxidation of the former by CO_2, yielding CO.[28] On the other hand, in the associative route, H_2 participates in the formation of intermediate species such as formate by the reaction with CO_2, and CO is formed by the decomposition of these intermediates.[29]

Under these premises, we have studied Pt/TiO_2 and Pt–Cs/TiO_2 catalysts for low-temperature RWGS. Herein, sub-nanometric Pt clusters close to single-atoms or isolated metal atoms dispersed on the solid support are intended to maximise the activity. The impact of Cs on the catalytic performance is discussed and thorough *operando* DRIFTS and UV-vis spectroscopy studies are performed shedding light on the different mechanistic routes and closing the debate about the role of Cs as a crucial promoter to deliver fully selective low-temperature RWGS catalysts.

2. Experimental details

2.1 Catalyst synthesis

The catalysts were synthesized by the wet impregnation method. For Pt/TiO_2, the necessary amount of H_2PtCl_6 to obtain 1 wt% Pt was dissolved in excess water. The TiO_2–P25 (Degussa) support was first washed with deionized water, filtered and calcined at 550 °C for 3 hours. Then, TiO_2 was impregnated in a rotary evaporator with a solution of platinum precursor salt until the solvent was removed until dryness. Then the sample was dried at 115 °C for 48 h, and finally calcined at 550 °C for 3 h.

For the synthesis of the Pt–Cs/TiO_2 catalyst, the required amount of Cs_2CO_3 was added to part of the Pt/TiO_2 sample, previously synthesised, to obtain 5 wt% of Cs. The solvent was then removed on a rotary evaporator and the sample was dried at 115 °C for 48 h. Finally, the catalyst was calcined at 550 °C for 3 h with a heating rate of 10 °C min^{-1}.

2.2 Characterization methods

X-Ray diffraction (XRD) measurements were carried out on an X'Pert Pro PANalytic diffractometer with a Cu-Kα anode at room temperature, working at a voltage of 45 kV and a current of 40 mA. Diffractograms were obtained over a 2θ range of 20°–90° with a step size of 0.05° and a step time of 300 s.

Raman spectroscopy measurements were carried out in a dispersive Horiba Jobin Yvon LabRam HR800 microscope equipped with a He–Ne green laser (532.14 nm) working at 5 mW, with a 600 g mm^{-1} grating. The microscope used a 50× objective and a confocal pinhole of 1000 μm. The Raman spectrometer was calibrated using a silicon sample reference.

The textural properties of the samples were analyzed by nitrogen adsorption–desorption measurements at liquid nitrogen temperature (77 K) in a Micromeritics Tristar II apparatus. Before the analysis, the samples were outgassed at 250 °C for 2 h.

High-resolution transmission electron microscopy (HR-TEM) and high-angle annular dark-field scanning transmission electron microscopy (HAADF-STEM) with element mapping analyses were performed on a FEI Talos F200S

Open Access Article. Published on 11 December 2023. Downloaded on 11/9/2025 9:25:01 AM. This article is licensed under a Creative Commons Attribution 3.0 Unported Licence.

electron microscope using an acceleration voltage of 200 kV with a field emission filament and a side-mounted Ceta 16M camera equipped with an energy dispersive X-ray analysis system (EDX X-Max 80T, Oxford Instruments). Prior to the analysis, the samples were *ex situ* reduced under the flow of 50% H_2/N_2 at 550 °C for 3 h and then a few milligrams of the reduced catalyst were deposited directly on a 300 mesh holey carbon coated copper TEM-grid and introduced under the microscope.

2.3 Catalytic activity tests

The catalytic activity measurements were performed under steady-state conditions in a fixed-bed quartz tubular reactor (i.d. 9 mm) working at atmospheric pressure and at three different temperatures (300, 400 and 500 °C) for 24 h at each one. In a typical procedure, the catalyst was crushed in the 100–200 μm particle size range and supported between two plugs of quartz wool in contact with a thermocouple. Prior to each test, the catalyst was reduced *in situ* under a flow of 10% H_2/N_2 (50 mL min^{-1}) at 550 °C for 1 h. The reaction mixture ($H_2/CO_2/N_2$) was fed with a H_2/CO_2 molar ratio of 4 and a high weight hour space velocity (WHSV) of 30 L g^{-1} h^{-1}. Reactants and reaction products were analysed by using an online gas chromatograph (Agilent 7890A) equipped with PPQ, MS-5A and SP-Sil 8 CB columns, and two TCD detectors and an FID detector. A coalescence filter coupled between FID and TCD modules was installed to avoid the presence of moisture in the GC columns. CO_2 conversion and CO/CH_4 selectivities were calculated by using the following equations:

$$CO_2 \text{ conversion } (\%) = \frac{\text{mol } CO_{2,in} - \text{mol } CO_{2,out}}{\text{mol } CO_{2,in}} \times 100 \quad (4)$$

$$\text{i selectivity } (\%) = \frac{\text{mol of i}}{\text{mol of CO} + \text{mol of } CH_4} \times 100, \text{ with i} = \text{CO or } CH_4 \quad (5)$$

Blank run tests were also performed in the absence of a catalyst and showed no conversion at the three reaction temperatures studied. In all the catalytic experiments conducted, the carbon balance in all catalytic experiments tally to 100% with an error within ±5%.

The ChemStations ChemCad software package was used to calculate the thermodynamic limits of the RWGS reaction at the studied temperatures. The Soave–Redlich–Kwong equation of state was used in a Gibbs reactor. Reactant inlet flows to the reactor are identical to the experimental parameters.

2.4 *Operando* DRIFTS measurements

Operando DRIFTS measurements were carried out using a reaction chamber (HVC-DRP, Harrick) mounted in a Praying Mantis (Harrick) DRIFTS optical system equipped with ZnSe windows. The spectra were collected using a Thermo Nicolet iS50 FTIR spectrometer equipped with an MCT detector in the range of 650–4000 cm^{-1} at 4 cm^{-1} resolution and an average of 64 scans per spectrum. The feed gas was controlled by using mass flow controllers (Bronkhorst). Before each experiment, the catalyst was activated at 400 °C with a flow of 50 mL min^{-1} of 10% H_2/Ar for 1 h. The surface reaction was evaluated at five different temperatures (150, 200, 250, 300 and 350 °C), holding each for 10 min and feeding a total flow of 50 mL min^{-1} (20 mL min^{-1} of H_2 and 5 mL min^{-1} of CO_2 balanced in argon). In addition, transient studies were also conducted to gain further insights into the intermediates involved in the reaction. To do so, alternated pulses of both reactants 40% H_2/Ar and 10% CO_2/Ar surfaces were successively switched after 5 min periods for each one.

2.5 *In situ* TPD-CO analysis

In situ TPD-CO followed by DRIFTS analysis of the calcined catalysts was performed using the same experimental system as that used for *operando* DRIFTS measurements. The spectra were recorded as an average of 64 scans with 4 cm^{-1} spectral resolution per spectrum. About 80 mg of finely ground calcined catalyst was loaded in the cell for each experiment and reduced *in situ* at 500 °C for 1 h with a flow of 10% H_2/Ar. Then, the sample was saturated under a flow of 50 mL min^{-1} of 5% CO/Ar at 50 °C and subsequently purged with Ar. The temperature-programmed desorption of CO (TPD-CO) was performed by feeding a flow of Ar (50 mL min^{-1}) and increasing the temperature from 50 °C to 400 °C at a rate of 5 °C min^{-1}. The spectra were recorded in continuous series mode using OMNIC 9.1 software and the temperature was simultaneously monitored.

2.6 *In situ* UV-visible analysis

In situ UV-vis experiments were carried out using a modified version of the CCR1000 reaction cell from Linkam Scientific Instruments (Fig. 1a). An emission-collection probe with six radiant optical fibers and one data collection optical fiber was placed inside the reaction cell for spectroscopic analysis. The experimental setup allows for modifying both the temperature of the reaction cell and the composition of the reactive atmosphere. The catalyst is placed in a ceramic bed perpendicular to

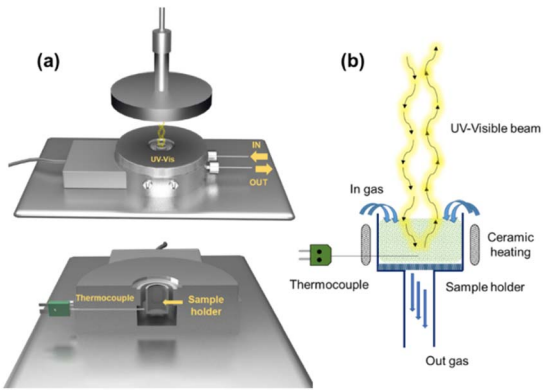

Fig. 1 (a) Scheme of the *in situ* UV–vis spectroscopic cell for catalyst characterization under reaction conditions and (b) schematic representation of the optical pathlengths of photons in the sample holder.

Open Access Article. Published on 11 December 2023. Downloaded on 11/9/2025 9:25:01 AM.
This article is licensed under a Creative Commons Attribution 3.0 Unported Licence.

the radiation beam, which enables gas flow through its bed (Fig. 1b).

The experiments were conducted under steady-state conditions in the range of 200–1000 nm. A commercial AVASPEC optical spectrometer (Avantes) with a DH-2000 lamp and a CCD detector was used. Barium sulfate was employed as the reference for analysis. The spectra were recorded by averaging 64 measurements with an integration time of 100 ms. The UV-vis operating experiments were conducted as follows: The temperature was gradually increased from 25 °C to 400 °C at a rate of 5 °C min^{-1}, whereas spectra were captured every 5 minutes. These measurements were carried out within a reducing atmosphere consisting of 10% H_2/Ar. Once the desired temperature of 400 °C was reached, the system was maintained at this temperature for 1 h under the same reducing atmosphere to ensure proper catalyst reduction. After the 1 h reduction period, the gas flow was switched from the reducing atmosphere to a reaction atmosphere composed of 10% CO_2, 40% H_2, and 50% Ar. This new gas mixture was maintained for an additional 60 minutes at a constant temperature of 400 °C. By following this experimental procedure, we were able to investigate and analyze the changes in the UV-vis spectra of the sample under different temperature and gas atmosphere conditions. These experiments provide valuable insights into the activity and selectivity of the studied RWGS catalysts.

3. Results and discussion

3.1 Structural and textural properties

Fresh samples were characterized by several physicochemical techniques to gather relevant information concerning structural and chemical properties of the design materials. Fig. 2a shows the normalized XRD patterns of Pt/TiO_2 and Pt–Cs/TiO_2 after calcination at 550 °C for 3 h. As can be observed, both catalysts show the typical diffraction lines of anatase (JCPDS 73-1764) and rutile (JCPDS 78-1510) phases. In both cases the tetragonal anatase phase is predominant. It is noteworthy that no diffraction signals corresponding to platinum species were detected in the XRD patterns of both Pt/TiO_2 and Pt–Cs/TiO_2 catalysts, although the platinum loading was 1 wt%, which

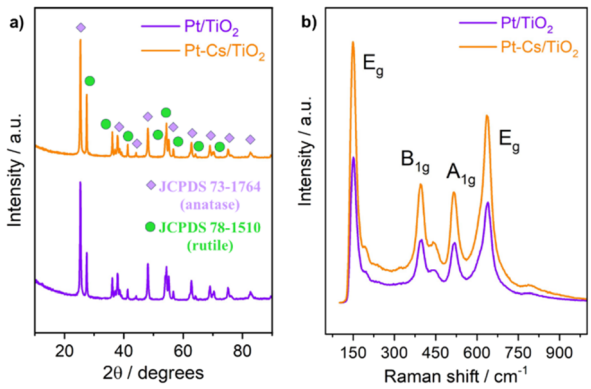

Fig. 2 (a) XRD patterns and (b) Raman spectra of both Pt/TiO_2 and Pt–Cs/TiO_2 catalysts after calcination at 550 °C in air.

Table 1 Textural properties of the TiO_2 support and Pt/TiO_2 and Pt–Cs/TiO_2 catalysts

Sample	S_{BET} (m^2 g^{-1})	Pore volume (cm^3 g^{-1})	Pore size (nm)	wt% Pt	wt% Cs
TiO_2 P25	45	0.39	29	—	—
Pt/TiO_2	38	0.31	25	0.6	—
Pt–Cs/TiO_2	40	0.29	24	0.8	4.8

emphasizes the small dimension of platinum particles which will be discussed later. Meanwhile, it must also be remarked that neither caesium phase was found in PtCs/TiO_2 suggesting that these species are highly dispersed on the support surface.

Fig. 2b shows the Raman spectra of both calcined catalysts. Note that both spectra are mainly constituted by four bands at 150, 360, 500 and 630 cm^{-1}, which are the four characteristic Raman active vibrational modes of the tetragonal anatase phase with symmetries E_g, B_{1g}, A_{1g} and E_g respectively. On the other hand, only one Raman active mode of the rutile phase, with symmetry E_g, can be observed at 450 cm^{-1} and shows a low intensity.[30] The features typical of rutile are less intense and they cannot be clearly assigned. Therefore, these results indicate that both catalysts are composed of a combination of anatase and rutile phases, anatase being the predominant phase. This observation is in concordance with the XRD results. Pt species and/or Cs phases are hardly detected by Raman spectroscopy.

Fig. S1† presents the N_2 adsorption–desorption isotherms of the calcined samples. Both catalysts are mesoporous materials with a type IV isotherm according to the IUPAC classification[31] and Cs does not seems to impact the overall textural features. Table 1 includes the specific surface area, total pore volume and pore size of fresh TiO_2 and the synthesized catalysts. Fresh TiO_2 surface area is 52 m^2 g^{-1} while Pt/TiO_2 and Pt–Cs/TiO_2 have a smaller surface area of 38 and 40 m^2 g^{-1}, respectively. Meanwhile, the pore volume and the pore sizes showed a similar decrease with the incorporation of Pt and Cs.

3.2 Verification of highly dispersed Pt clusters

Fig. 3a and b illustrate the HRTEM micrographs of both reduced Pt/TiO_2 and Pt–Cs/TiO_2 catalysts. As can be observed, the crystallographic plane spacing of both rutile (101) and anatase (101) tetragonal phases is 2.52 and 3.54 Å, respectively, for both samples suggesting that the presence of Cs does not affect the crystal structure of TiO_2. The absence of crystal planes related to caesium phases in Pt–Cs/TiO_2 suggests that this element could be dispersed forming surface amorphous phases. On the other hand, it can be noticed that both samples comprise isolated Pt sites or sub-nanoclusters smaller than 0.5 nm in diameter (circles marked in Fig. 3a and b). As this is the case, we can hardly estimate the average particle size of the Pt sub-nanometric particles in any sample. HAADF-STEM images (Fig. S2 and S3†) prove the existence of highly dispersed Pt on a TiO_2 support without obvious aggregation of Pt atoms in both reduced catalysts. It is also evident that caesium is well dispersed on the Pt–Cs/TiO_2 catalyst (Fig. S3†).

 This journal is © The Royal Society of Chemistry 2024

Open Access Article. Published on 11 December 2023. Downloaded on 11/9/2025 9:25:01 AM.
This article is licensed under a Creative Commons Attribution 3.0 Unported Licence.

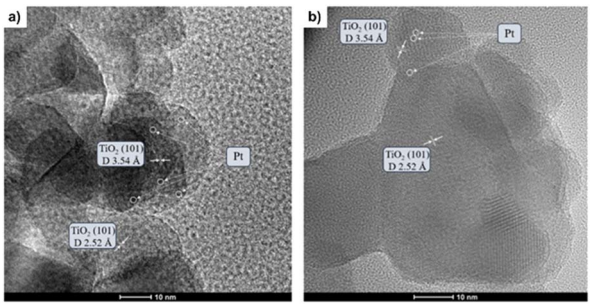

Fig. 3 HR-TEM micrographs of both Pt/TiO_2 (a) and $PtCs/TiO_2$ (b) catalysts reduced at 550 °C in 50% H_2/N_2 for 3 h.

The results obtained reveal the presence of subnanometric Pt clusters or isolated Pt sites with an excellent dispersion over the support for both prepared catalysts confirmed by the mapping compositional presented in Fig. S2 and S3.† In addition to this, Table 1 also includes the Pt and Cs percentages obtained by EDX analysis and the values obtained are very close to the nominal ones confirming the metallic and promoter contents in the final catalysts.

3.3 RWGS catalytic performance

The as-prepared catalysts were evaluated in the reverse water–gas shift (RWGS) reaction. The catalytic activity was recorded at different temperatures (300, 400 and 500 °C) for 24 h at each temperature. First, CO_2 conversion of Pt/TiO_2 and $Pt–Cs/TiO_2$ is shown in Fig. 4a. At higher temperatures (400 and 500 °C), a slightly higher CO_2 conversion for the un-promoted catalyst is evidenced while at low temperature (300 °C) similar conversions were reached for both catalysts. From Fig. 4a, it is interesting to note that the conversion of $Pt–Cs/TiO_2$ decreased drastically from 26 to 21% during the first 3 h and then only decreased very slowly. One of the possible reaction mechanisms for RWGS involves CO_2 adsorption on the basic sites of the support followed by a reaction to form carbonate species and the subsequent reduction of these to CO.[22] In agreement with the literature, the presence of basic sites such as Cs dispersed on the support leads to the formation of active carbonates that require higher temperatures to be reduced, and the saturation of these sites could explain the initial decrease in the conversion. As will be discussed later in the manuscript, the Cs sites in the vicinity of Pt sub-nanoclusters play a key role in the reaction pathway. Herein, the most interesting observation is related to the CO selectivity as shown in Fig. 4b. Our Cs-doped systems reach 100% selectivity towards CO at very low temperatures (300–400 °C) and 95% selectivity towards CO is reached at 500 °C. In contrast, the selectivity of the non-doped catalyst slightly decreases with the temperature (Fig. 4b). We can then infer that the addition of Cs has a strong impact on the end-product distribution and provokes a remarkable shift in the selectivity. Let us recall at this point that the expected trend would have been a high selectivity in the low-temperature range due to the

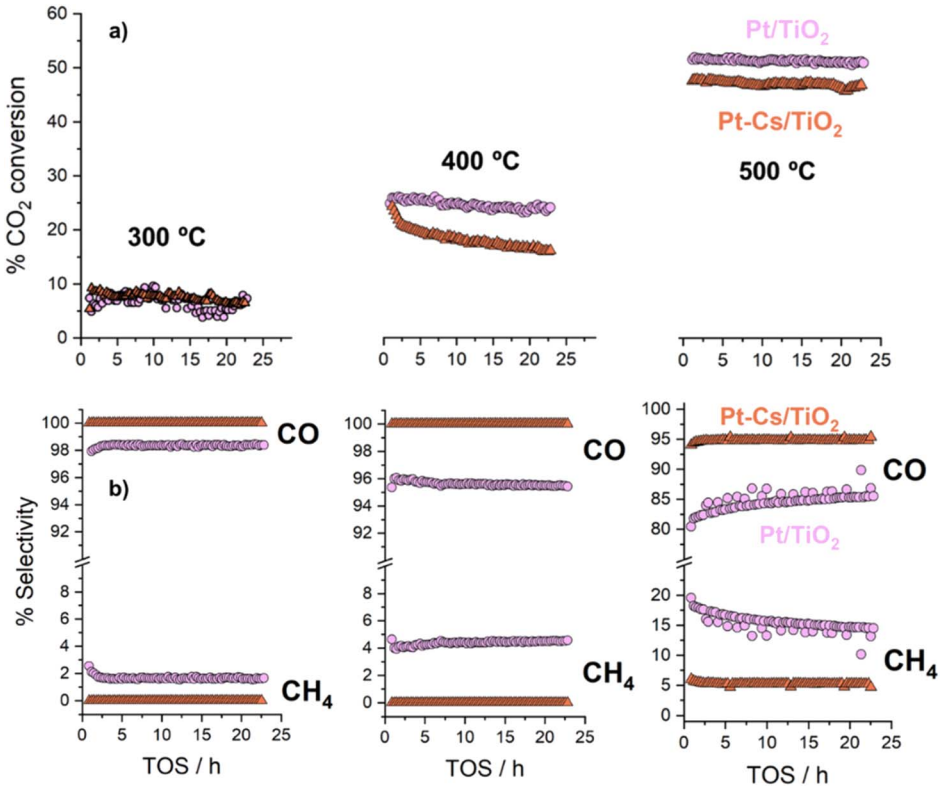

Fig. 4 Catalytic activity of Pt/TiO_2 and $Pt–Cs/TiO_2$ catalysts for RWGS in terms of CO_2 conversion (a) and selectivity (b) as a function of the time-on-stream and the temperature. Reaction conditions: $H_2/CO_2 = 4$, $P = 1$ bar, and WHSV = 30 L g^{-1} h^{-1}.

Open Access Article. Published on 11 December 2023. Downloaded on 11/9/2025 9:25:01 AM.
This article is licensed under a Creative Commons Attribution 3.0 Unported Licence.

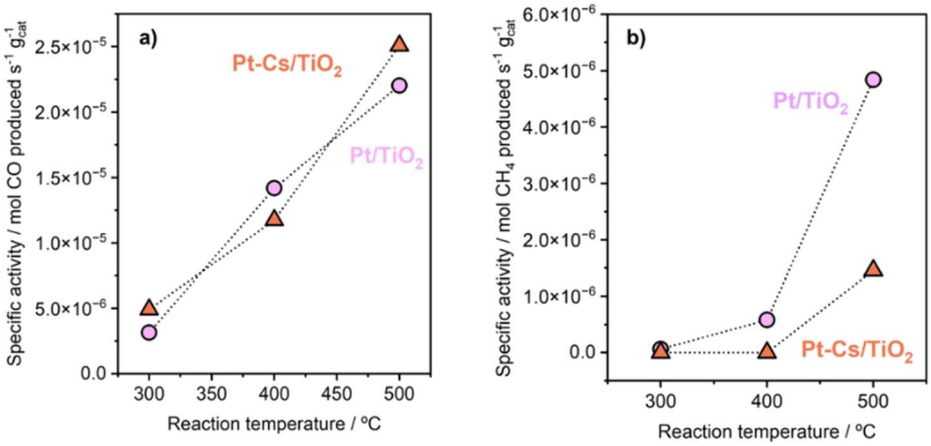

Fig. 5 Specific activity of Pt/TiO_2 and $Pt–Cs/TiO_2$ catalysts for RWGS in terms of production of (a) CO and (b) methane. Reaction conditions: $H_2/CO_2 = 4$, $P = 1$ bar, and WHSV = 30 L g^{-1} h^{-1}.

predominance of CO_2 methanation which is an exothermic reaction. Our outstanding CO selectivity clearly associated with Cs as the dopant is a highly commendable result opening the horizons for a new family of 100% CO-selective catalysts that can be implemented in RWGS units running at as low as 300 °C. Such a strategy results in a formidable impact in terms of process cost saving (lower CAPEX and OPEX).

The promoter effect can be better noticed in Fig. 5a and b where the specific activity to CO and CH_4, respectively, of both catalysts is presented. In addition, space-time yield (STY) for Pt/TiO_2 and $PtCs/TiO_2$ has been calculated (Fig. S4†). While both catalysts present a similar production of CO (1.86 and 1.88 mol of CO per s per m^3 at 500 °C, respectively), for the production of CH_4 the difference is more evident (0.33 and 0.11 mol of CH_4 per s per m^3 at 500 °C). These results are in fair agreement with previous studies where alkali metals weaken the CO–surface interaction, hindering further hydrogenation of CO to CH_4.[32–34] Furthermore, Zhao *et al.*[11] studied how Pt particle size and dispersion affect the CO selectivity, concluding that Pt species with large sizes exhibited stronger adsorption towards CO than atomically dispersed Pt species favouring the hydrogenation of CO to CH_4. Even though the Pt particle size of both catalysts is similar revealing the presence of sub-nanometric Pt clusters getting close to single atom domains, it can be seen in Fig. 5 that the addition of Cs seems to inhibit CH_4 formation. Silva *et al.*[35] attributed this effect to the strong interaction that is formed between reduced platinum and basic caesium oxide species.

3.4 Elucidating the reaction intermediates: *operando* DRIFTS studies

Within the aim of investigating the involved surface species and obtaining relevant aspects of the RWGS mechanism, the surface reaction was evaluated under working conditions by means of DRIFTS measurements. For the sake of consistency, the reaction conditions used in the *operando* analysis were analogous to those used in a conventional fixed-bed reactor.

Fig. S5† presents the DRIFTS spectra obtained for both catalysts after activation under 50 mL min^{-1} of 10% H_2/Ar at 400 °C for 1 h. It is remarkable that the addition of Cs neutralizes all the surface hydroxyl groups (bands at 3716 cm^{-1} and 3670 cm^{-1}) of TiO_2. This first piece of evidence suggests that the reaction pathways must be different for both catalysts (*vide infra*). Fig. 6 shows the evolution of the spectra for Pt/TiO_2 under reaction conditions in the 150–350 °C temperature range. As can be noticed in Fig. 6a, the region of hydroxyl groups (3800–3500 cm^{-1}) is characterized by the disappearance of five different features related to hydroxyls bonded to Ti^{4+} and Ti^{3+} with different coordination. The bands at 3716 cm^{-1} and 3688 cm^{-1} are presumably attributed to isolated terminal OH groups, while the bands at 3624 cm^{-1}, 3596 cm^{-1} and 3414 cm^{-1} are typical of OH groups bonded forming bridges.[36] Furthermore, the band at 3670 cm^{-1} is associated with OH bonded to Ti^{3+}, and it is noteworthy that it disappears with the increase in temperature while the band at 3688 cm^{-1}, associated with OH bonded to Ti^{4+} simultaneously increases. This clearly reveals that oxygen vacancies are formed on titania in good agreement with the literature.[27]

On the other hand, the bands located in the region between 2080 and 2060 cm^{-1} correspond to CO adsorbed on different Pt active sites.[37] Stakheev *et al.*[38] studied the electronic state and localization of supported Pt atoms by CO adsorption. These authors reported that the bands at 2078 and 2059 cm^{-1} are related to CO linearly adsorbed on accessible Pt sites composed of only a few atoms involving different degrees of metal–support interaction or different particle geometries. As shown in Fig. 6b, these bands shift to lower frequencies with the increase in temperature. It is noteworthy that the intensity of the CO bands hardly decreases with the temperature suggesting that these CO peak redshifts cannot be attributed to the CO coverage. We believe that this bathochromic peak shift is mainly related to the formation of oxygen vacancies and the transfer of electrons to the Pt particles. When the temperature is increased, electrons in the valence band of titania are transferred to the conduction band generating holes in the valence band. Then these

 This journal is © The Royal Society of Chemistry 2024

Open Access Article. Published on 11 December 2023. Downloaded on 11/9/2025 9:25:01 AM.
This article is licensed under a Creative Commons Attribution 3.0 Unported Licence.

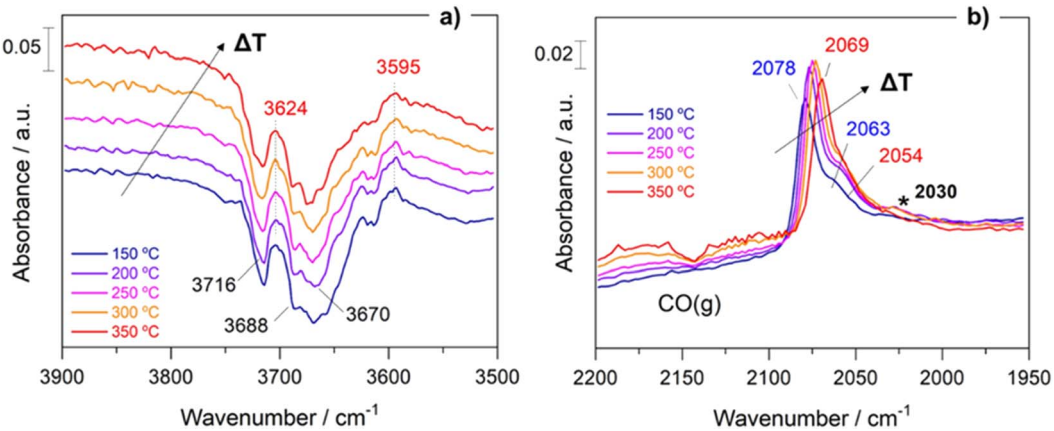

Fig. 6 Evolution of DRIFTS spectra with the temperature under reaction conditions for the Pt/TiO_2: hydroxyl region (a) and carbonyl region (b). Reaction conditions: 5/20/25 mL min^{-1} of $CO_2/H_2/Ar$, WHSV = 30 L g^{-1} h^{-1} and 1 bar.

electrons can be transferred to Pt atoms located on the metal/support interface weakening the C–O bond and shifting the CO bands to lower wavenumbers without decreasing the intensity. A similar observation was reported by Shuai Shen *et al.*[39] but in this study the electron transfer was induced by light radiation instead of temperature increment. Furthermore, the appearance of another band at 2030 cm^{-1} above 250 °C is also remarkable. This feature is related to the presence of CO adsorbed on electron-rich Pt sites in which carbon overlayers were deposited.[40] The presence of this band indicates that CO can be dissociated into C* and O* creating carbon deposits on the Pt particles, and the hydrogenation of C* to form CH* species is responsible for the production of methane. This way we explain the production of methane in the Pt/TiO_2 catalyst, a phenomenon that can be ruled out at low temperatures when Cs is added as the promoter.

In an analogous manner, Fig. 7 displays the evolution of the spectra of Pt–Cs/TiO_2 under working conditions as a function of the reaction temperature. The most important difference found for this catalyst was the absence of hydroxyls. Fig. 7a shows the presence of bands in the 2100–1900 cm^{-1} region, indicating the formation of carbonyl adsorbed species. The band at 2063 cm^{-1} is typically ascribed to CO linearly adsorbed on Pt sites and this band disappears progressively as reaction temperature increases. In this case, the bathochromic shift is mainly related to the lower coverages of CO when the reaction temperature is increased. On the other hand, Fig. 7a evidences the emergence of two bands at 2033 and 1998 cm^{-1} when the temperature is increased above 300 °C. These two bands are ascribed to carbonyl adsorbed species on Pt sites covered by carbon deposits and explain the formation of small amounts of methane at higher temperatures in agreement with the catalytic results (Fig. 5). It should be mentioned that the CO stretching vibrations observed in the Cs-promoted sample appear at lower frequency than that of the unpromoted sample. This fact is related to the back donation effect of Cs in intimate contact with

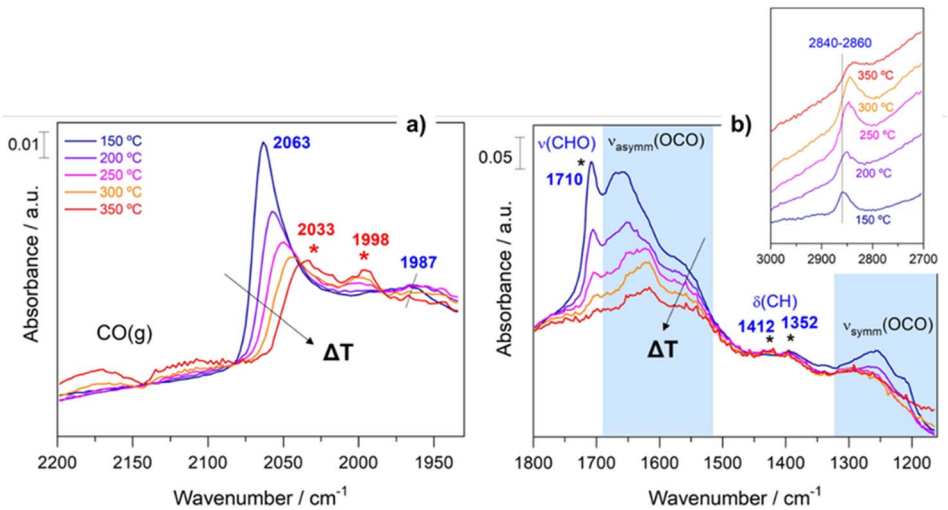

Fig. 7 Evolution of DRIFTS spectra with the temperature under reaction conditions for the Pt–Cs/TiO_2: carbonyl region (a) and carbonate region (b). Reaction conditions: 5/20/25 mL min^{-1} of $CO_2/H_2/Ar$, WHSV = 30 L g^{-1} h^{-1} and 1 bar.

Open Access Article. Published on 11 December 2023. Downloaded on 11/9/2025 9:25:01 AM.
This article is licensed under a Creative Commons Attribution 3.0 Unported Licence.

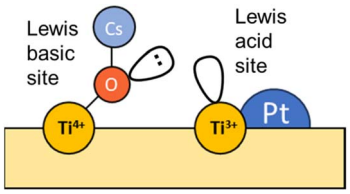

Fig. 8 Representation of a frustrated Lewis pair (FLP) on Pt–Cs/TiO_2.

Pt atoms.[41] Due to the ionic ratio of Cs, it may be assumed that caesium species are located on the perimetric sites of Pt particles and dispersed on the support. Moreover, the presence of a band at about 1987 cm^{-1} can be observed at lower temperatures, whose presence requires a more detailed explanation. This feature is ascribed to CO adsorbed on very small Pt clusters.[42] Calabrese *et al.*[43] reported that platinum carbonyl cluster dianions of general formula $[Pt_3(CO)_3(\mu_2\text{-}CO)_3]_n^{2-}$ (n = 2, 3, 4 and 5) present a characteristic IR band at this frequency. The HRTEM micrographs (Fig. 3) revealed that Pt particles are smaller than 1 nm (around 20 atoms) suggesting that the presence of a platinum dimers or trimers cannot be discarded. Remarkably, this feature was hardly observed in the unpromoted catalyst suggesting that the presence of caesium stabilizes the formation of platinum carbonyl cluster dianions. Recently, Li *et al.*[44] reported that dual-active sites composed of Pt clusters and frustrated Lewis pairs (FLPs) can be created on the surface of CeO_2 to boost the performance of RWGS at low temperatures. In another recent study, Jeong-Cheol Seo *et al.*[45] suggested by means of *operando* FTIR and density functional theory (DFT) calculations that FLPs can be formed in Pt/Na-zeolite catalysts and these centres could effectively stabilize the intermediate responsible for CO production in the RWGS reaction. Hence, the concept of "surface frustrated Lewis pairs" refers to proximal Lewis acid–Lewis base sites occurring on metal oxide surfaces, which have been reported in the literature to be responsible for driving diverse heterogeneous catalytic reactions.[46] In this line, we believe that surface FLPs constituted by Cs–O–Ti^{4+} (Lewis base) sites and Ti^{3+} (Lewis acid) are presumably created at the metal/support perimeter in which titania is highly defective as depicted in Fig. 8. Ghuman *et al.*[47] demonstrated that oxygen vacancies are required to form these surface FLP sites, and they are highly efficient to simultaneously dissociate H_2 and activate CO_2 molecules. The reduction of CO_2 leads to CO adsorbed on FLPs, which is faster for recovering the active sites and preventing further hydrogenation to CH_4.[44,45] In other words, Cs is acting not only as an electronic dopant but also as a structural promoter favouring highly dispersed Pt nanoclusters and ultimately boosting the selectivity in RWGS at low temperature. At higher temperatures, the energy barrier for CO dissociation is overcome, and methane formation cannot be inhibited. Furthermore, Fig. 7b shows the formation of carbonate species at lower temperatures evidenced by the features appearing between 1650 and 1500 cm^{-1} and 1300–1100 cm^{-1}, which are related to symmetric and asymmetric stretching of –OCO carbonate species, respectively.[48] It is well-known that Cs is an alkaline species that increases the surface basicity of the material and, consequently, tends to form carbonate like-compounds.[32] As mentioned above, Cs remarkably neutralizes all hydroxyl groups. It is well known that formate species are formed by reduction of bicarbonate species, and bicarbonate formation involves the reaction of CO_2 with OH. Therefore, the formate route must be apparently ruled out as a possible mechanism of RWGS for Pt–Cs/TiO_2.

On the other hand, new species have been detected and proposed as intermediates in this study. Fig. 7b shows bands initially observed at 2840–2860 (Fig. 7b inset), 1710, 1410, and 1352 cm^{-1} emerging simultaneously. These vibration modes are related to C–H stretching, C=O stretching, CHO scissors and C–H flexions, respectively. These features may be assigned to oxygenated adsorbed species (–CHO) such as acyl or acetyl species.[49] Moreover, it is evident that these species undergo some structural changes and at higher temperatures are decomposed into CO. This fact could be explained by means of the following sequence: CO*–H* → formyl → acyl → CO gas. The experimental evidence of these intermediates is fundamental to establish a pathway route. So far, these species have been proposed by means of density functional theory (DFT) calculations,[50] but they have hardly been experimentally observed. The formation of oxygenated compounds *via* insertion of carbonyl has been proposed for Pt based catalysts in CO hydrogenation, so it is reasonable to expect that these intermediates can be formed.[51] Furthermore, an increase in the pressure likely leads to the formation of oxygenated compounds against CO, and this opens a new horizon for the production of oxygenated compounds such as alcohols, ketones, carboxylic acids, *etc.*

In order to confirm the formation of a –CHO like intermediate in the RWGS reaction, transient studies by switching CO_2 and H_2 streams were performed. This study provides relevant information on the reaction intermediates since the reaction is carried out under non-steady state conditions, thus extending the reaction intermediate lifetime. For this purpose, the reaction temperature was fixed at 300 °C to ensure low conversions and high surface concentration of intermediate species. Fig. 9a displays the temporal evolution of DRIFT spectra for Pt/TiO_2 when both reactants are switched each 5 min. As can be noticed, the introduction of CO_2 leads to the formation of new features in the carbonyl region (2100–1900 cm^{-1}). These bands correspond to carbonyl adsorbed species with different coordination on Pt particles as discussed above. It should be noted that during the reduction step the carbonyls at 2075, 2054 and 2030 cm^{-1} are released much faster than the carbonyl at 2069 cm^{-1}. This reveals that the latter is more strongly adsorbed and likely acts as an intermediate for methane formation. On the other hand, it is also evident that the hydroxyl species (band in the 3800–3500 cm^{-1} range) are also contributing to the reaction. However, the identification of these bands is not straightforward since they are masked by gas-phase CO_2 combination bands ($2\nu_2 + \nu_3$ and $\nu_1 + \nu_3$). Thus, these observations reveal that CO_2 is dissociated into CO* and O* on the HO-□-Ti^{3+} sites, being □ an oxygen vacancy which is oxidized by O*. Then when the CO_2 feed is substituted by the H_2 feed, molecular hydrogen is dissociated into 2H* on Pt sites, and H*

Open Access Article. Published on 11 December 2023. Downloaded on 11/9/2025 9:25:01 AM.
This article is licensed under a Creative Commons Attribution 3.0 Unported Licence.

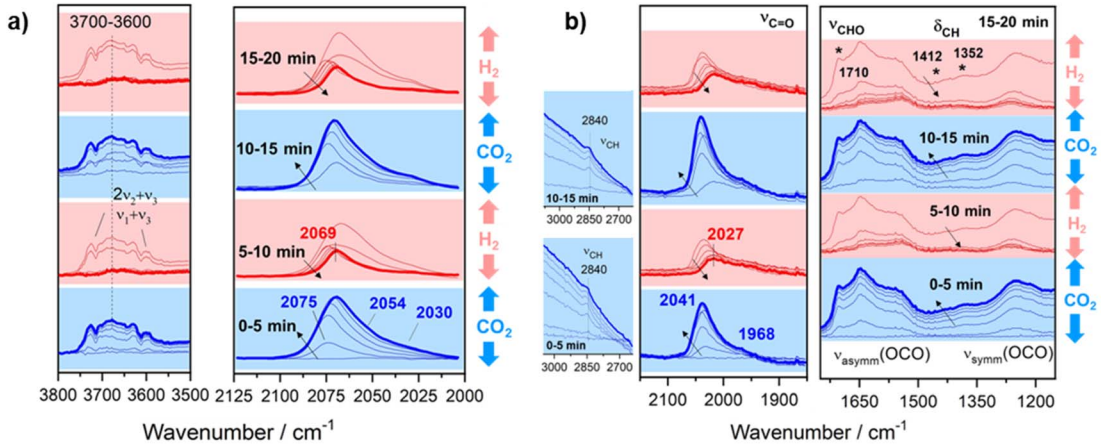

Fig. 9 Temporal evolution of DRIFT spectra on (a) Pt/TiO_2 and (b) Pt–Cs/TiO_2 catalysts by switching 50 mL min^{-1} 10% H_2/Ar and 50 mL min^{-1} 10% CO_2/Ar each 5 min at 300 °C.

migrates by spill over phenomena recovering the HO-□-Ti^{3+} sites for a new cycle. It is also noticed that the bands associated with more labile Pt carbonyls disappeared and CO gas is released. Likewise, strongly adsorbed Pt carbonyl is able to dissociate C into C* species which are further hydrogenated into methane or built up in the metallic sites. Thus, it cannot be ruled out that Pt sites are covered by a layer of C* species after multiple cycles.[52]

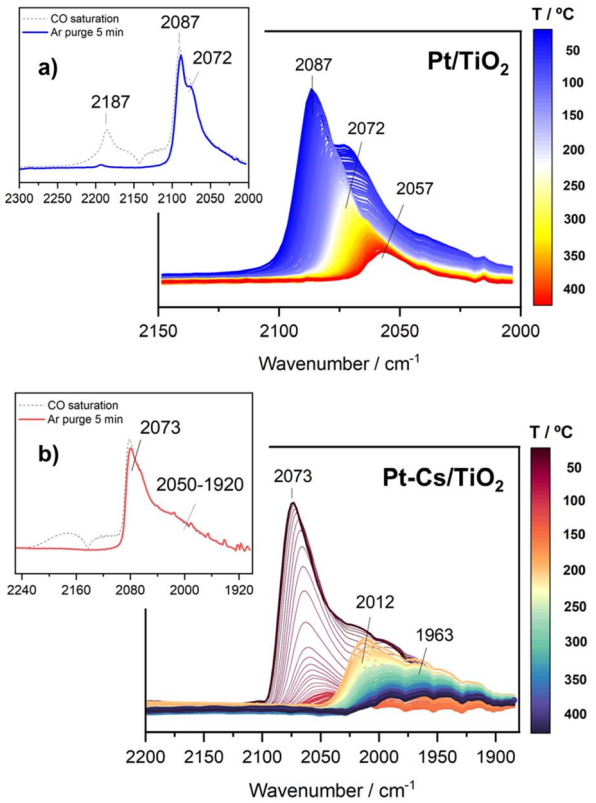

Fig. 10 Evolution of DRIFT spectra with the temperature during the TPD-CO experiment in both catalysts (a) Pt/TiO_2 and (b) Pt–Cs/TiO_2 catalysts. The inset of the figures includes the spectra after CO saturation at 50 °C and after purging with Ar for 5 min.

Concerning the Pt–Cs/TiO_2 catalyst, Fig. 9b shows the temporal evolution of DRIFT spectra during successive switching of both H_2 and CO_2 reactants over the Cs-promoted sample. It can be observed that under a 10% CO_2/Ar stream caesium carbonates (1650–1200 cm^{-1}) and Pt carbonyl species (bands at 2100–1900 cm^{-1}) are formed. On the other hand, the emergence of the bands attributed to the above formyl/acyl species (2841, 1794, 1420 and 1392 cm^{-1}) is also observed. This reveals that, effectively, these species are intermediates of the RWGS reaction on Cs-promoted samples. When H_2 is introduced, all these oxygenated species disappeared, and CO gas is released. However, a band at 2027 cm^{-1} still remains after 5 min of reduction. As mentioned above for the unpromoted catalyst, this band corresponds to carbonyls more strongly adsorbed on Pt sites and this intermediate can be further dissociated or hydrogenated into methane at higher temperatures. On the basis of these results, we can conclude that at low temperatures Cs promotes two possible reaction pathways: the (i) formyl/acyl pathway, in which –CHO species are formed and evolve to CO gas, and (ii) frustrated Lewis pair assisted CO_2 reduction route, in which FLPs induce the heterolytic dissociation of H_2 and the subsequent hydrogenation of CO_2 to CO. Although caesium carbonates are also formed during the reaction at lower temperatures, we have observed that the specific activity of CO production in both catalysts is identical (Fig. 5a). This indicates that these carbonates cannot be reduced to CO in Pt–Cs/TiO_2 and thus these species are mere spectators.

3.5 *In situ* TPD-CO followed by DRIFTS analysis

In situ TPD-CO followed by DRIFTS analysis was carried out to obtain information about the desorption behaviour of CO in both catalysts. For this purpose, the activated catalysts were saturated with CO at 50 °C and subsequently purged with Ar. The evolution of the IR spectra with the desorption temperature is shown in Fig. 10a and b. As can be observed in the inset of

Open Access Article. Published on 11 December 2023. Downloaded on 11/9/2025 9:25:01 AM.
This article is licensed under a Creative Commons Attribution 3.0 Unported Licence.

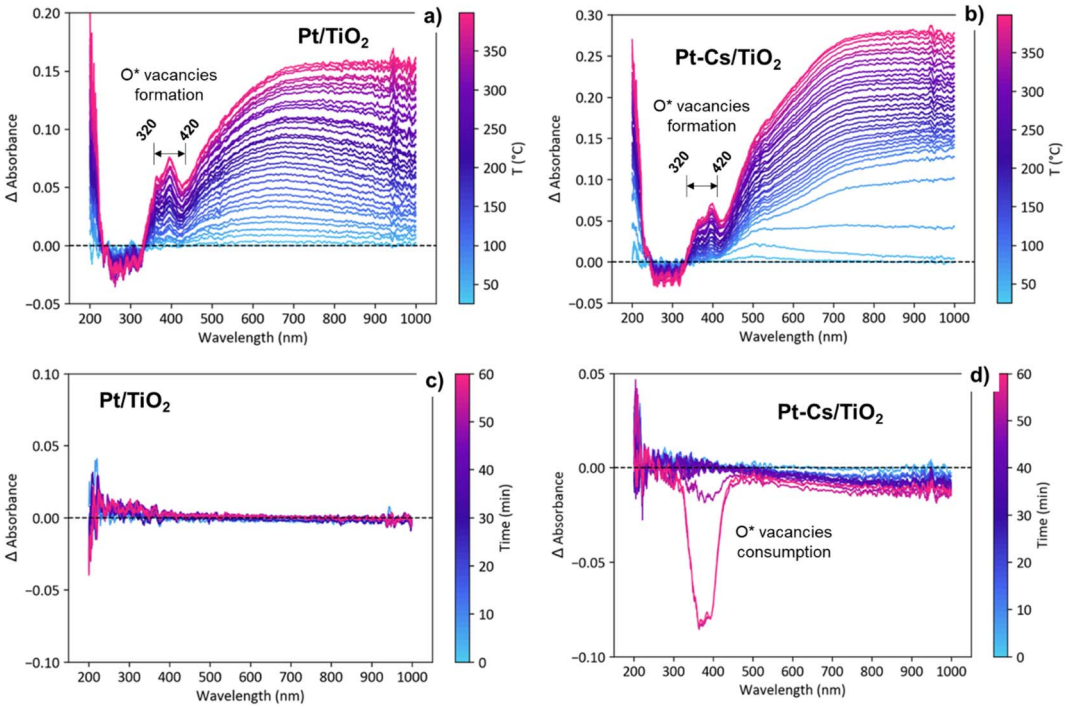

Fig. 11 Evolution of difference UV-vis spectra as a function of the temperature during the activation pretreatment in a flow of 10% H_2/Ar (a and b) and as a function of the time during the RWGS reaction (5/20/25 mL min^{-1} of CO_2/H_2/Ar, WHSV = 30 L g^{-1} h^{-1} and 1 bar) at 400 °C (c and d) for both catalysts.

Fig. 10a, the Pt/TiO_2 sample is mainly characterized by two intense bands at 2087 and 2012 cm^{-1}. As mentioned above, these bands correspond to CO linearly adsorbed on Pt active sites with different shapes and/or geometries. A band at 2187 cm^{-1} was also found which decreased significantly after purging with Ar for 5 min. This feature is related to CO adsorption forming one type of Ti^{4+}–CO carbonyls.[53] From Fig. 10a, it is noteworthy that both bands at 2087 and 2072 cm^{-1} disappeared progressively as temperature increased and a band at 2057 cm^{-1} remained. As stated above, this band corresponds to CO adsorbed on electron-rich Pt sites surrounding carbon overlayers formed by CO dissociation.[40]

Concerning the doped Pt–Cs/TiO_2 catalyst, the inset of Fig. 10b displays the IR spectra recorded after CO saturation and Ar purging for 5 min at 50 °C. Remarkably, this catalyst does not show the band at high wavenumber (2184 cm^{-1}) characteristic of CO adsorbed on acidic Lewis sites. This fact is attributed to the neutralization of acidic sites with the introduction of caesium. Furthermore, the spectra show a high intensity peak at 2073 cm^{-1} with a wide shoulder at 2050–1920 cm^{-1}. The more intense band is ascribed to CO linearly adsorbed on Pt sites.[39] One can notice that this band disappeared completely above 150 °C (Fig. 10b). In comparison to the unpromoted sample, this CO stretching vibration appears at a lower frequency due to the back donation effect of Cs in intimate contact with Pt atoms.[41] Likewise, it should be stressed that the broad band (2050–1920 cm^{-1}) also disappeared at 150 °C but it emerges again progressively as the temperature increases. The formation of these species within the studied temperature can be attributed to carbonate decomposition on caesium sites (not shown in Fig. 10b). These bands remain stable until 350 °C, and then their intensity decreases with temperature. It is noteworthy that even at 400 °C these bands are still present on the surface. In agreement with the latter discussion, this set of bands is attributed to CO adsorbed on very small Pt clusters which are thermally very stable. Based on these observations, we can conclude that the presence of caesium stabilizes small particles of platinum and avoids the dissociation of CO into carbonaceous species.

3.6 Role of vacancies: *in situ* UV-visible analysis

Fig. S6† displays the evolution UV–vis spectra for both catalysts during activation in 10% H_2 as a function of the temperature and under RWGS reaction conditions at 400 °C as a function of the reaction time. As shown in Fig. S6a and b,† during the activation process in 10% H_2/Ar, a new band emerges between 320 and 420 nm indicating the reduction of Ti^{4+} to Ti^{3+} and thus the formation of oxygen vacancies.[54] To emphasize these changes, Fig. 11a and b present the evolution of the difference spectra with temperature during the activation pretreatment for both catalysts. The spectrum recorded at 25 °C was taken as the reference. Note that an increasing level of formation of oxygen vacancies was evidenced during heating to 400 °C, supported by the intensity increase of a positive band in the 320–420 nm region, suggesting a bandgap modification related to the contribution of the formed Ti^{3+} levels.[27] These changes associated with the formation of oxygen vacancies are evident in both

Open Access Article. Published on 11 December 2023. Downloaded on 11/9/2025 9:25:01 AM.
This article is licensed under a Creative Commons Attribution 3.0 Unported Licence.

catalysts (Fig. 11a and b), exhibiting a comparable intensity increase. This similarity suggests that the formation of vacancies occurs in both catalysts to a similar extent during the reduction pretreatment.

On the other hand, the emergence of a broad band ranging from 500 to 800 nm, extending into the near-IR zone (Fig. 11a and b), is ascribed to the surface plasmon resonance (SPR) effect of metallic particles.[55] This phenomenon occurs as a result of the collective resonance of small Pt clusters, aligning with the tiny clusters observed through HRTEM (Fig. 3). The slight bathochromic shift observed during the reduction process in the Pt–TiO_2 catalyst is associated with the coalescence of neighbouring small Pt-clusters, forming slightly larger aggregates.[56,57] Nevertheless, the lack of band displacement over time during 1 h in s reduction atmosphere at 400 °C (not shown) affirms the stability of the presumably formed nanoparticles due to the Pt–TiO_2 strong metal support interaction effect (SMSI effect).[58]

The transition from the activation (H_2/Ar) to reaction stream (H_2/CO_2/Ar) leads to distinct evolutions of the UV-vis spectra in both catalysts. As shown in Fig. S6c† and 11c, the Pt–TiO_2 catalyst exhibits no discernible changes in the spectra when exposed to the reaction atmosphere. This observation implies that oxygen vacancies are being consumed and cyclically regenerated. This hypothesis aligns with the results obtained from DRIFTS. Furthermore, the lack of evolution in the Pt-plasmon suggests long-term stability of the platinum clusters. By contrast, upon introducing caesium to the catalyst, oxygen vacancy consumption is observed during prolonged reaction times with an intensity comparable to that associated with vacancy formation (Fig. S6d† and 11d). The decrease in band intensity at extended reaction times suggests vacancy consumption and an inefficient regeneration process. At shorter reaction times, vacancies are likely playing an active role in the reaction due to their initial formation.[41] Eventually, the vacancies become blocked, compelling the reactive pathway to follow an alternative mechanism. In agreement with the *operando* DRIFTS results, these observations are consistent with the proposed formation of frustrated Lewis pairs, which requires the presence of oxygen vacancies as active centers for dissociating H_2 and reducing CO_2 into CO. The selectivity of the reaction is closely related to the catalyst's ability to activate H_2 and CO_2 molecules, as well as the mechanistic pathway followed. The catalyst's propensity to donate electron density to the reactants directly influences its performance in the reaction. Alkali promoters have a high tendency to form surface titanates, which exhibit a more insulating character compared to P25 titania. By employing the Tauc plot method,[59] the calculation of the band gap indicates a 0.1 eV difference between the two catalysts before activation (Fig. S7†). This discrepancy

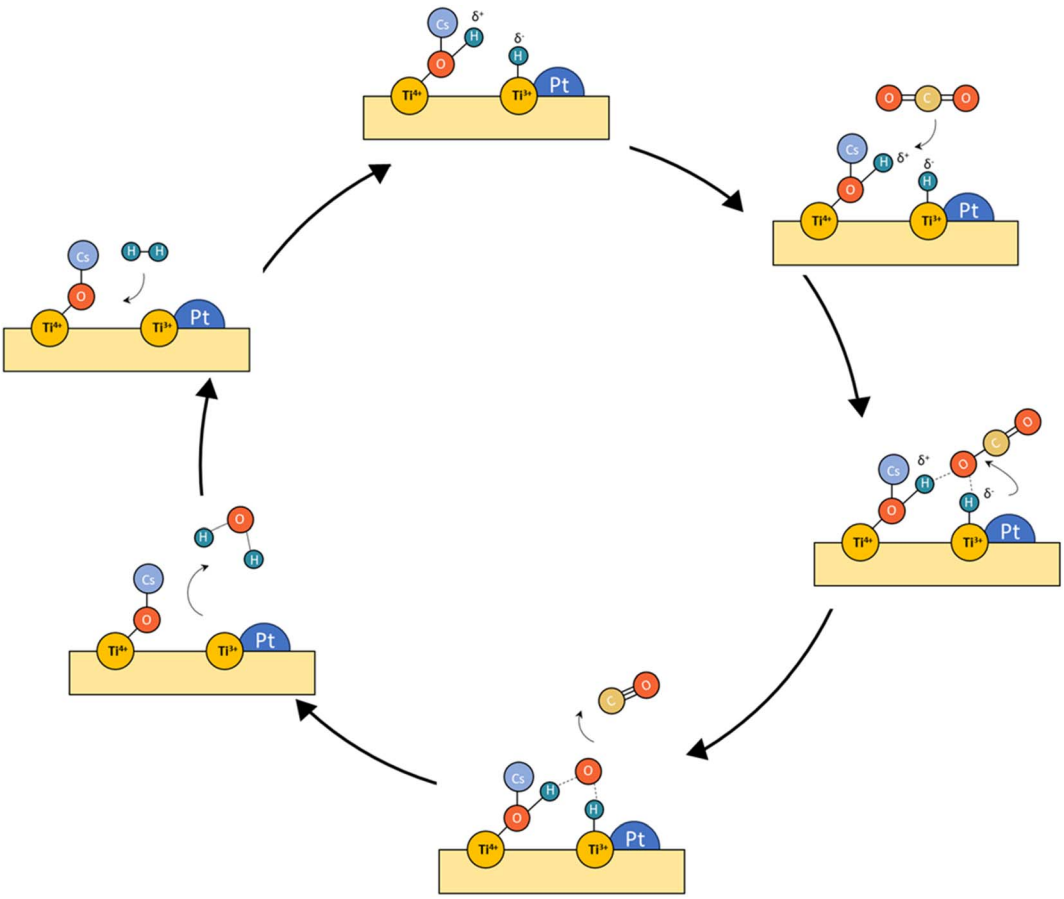

Fig. 12 Tentative reaction mechanism proposed for the concept of frustrated Lewis pairs (LFPs) for Pt–Cs/TiO_2.

Open Access Article. Published on 11 December 2023. Downloaded on 11/9/2025 9:25:01 AM.
This article is licensed under a Creative Commons Attribution 3.0 Unported Licence.

highlights the insulating effect resulting from caesium doping in the catalyst. This consistent disparity, observed throughout the activation and reaction processes, aligns with the formation of methane. The formation of methane relies on a catalyst with enhanced conductivity to facilitate both CO_2 activation and H_2 spillover. The addition of caesium further enhances the insulating nature of the catalyst, thereby diminishing its hydrogenation capacity and favouring the CO desorption. The smaller band gap of Pt–TiO_2 is directly related to higher catalyst activity towards CO dissociation and subsequent hydrogenation of C* into methane.

3.7 Mechanistic insights

From these observations, we deduce the reaction schemes shown in Fig. 12 for both catalysts. In the case of Pt/TiO_2, platinum particles are firmly anchored on the surface of titania under the reaction conditions due to the interaction between Pt and TiO_2, through which abundant stable active sites are available. Furthermore, active surface oxygen vacancies were *in situ* generated and consumed circularly during the reaction, which facilitated the activation of CO_2 and improved the catalytic efficiency. This pathway corresponds to the classical redox mechanism. However, the possible formation of carbon layers can be a cause of deactivation that requires a stability study.

Concerning the Pt–Cs/TiO_2 catalyst, it must be stated that two possible routes are possible: the (i) formyl/acyl pathway, in which –CHO species are formed and, depending on the reaction conditions, evolve to CO gas or oxygenated compounds and (ii) frustrated Lewis pair assisted CO_2 reduction, in which FLPs are formed between Cs–O–Ti^{4+} sites and Ti^{3+} at the metal/support peripheral sites. These FLP sites are highly active to heterolytically dissociate hydrogen on the Pt clusters with high electronic density, and CO_2 can be easily activated on the Cs–O–Ti^{3+} basic sites. In this case, the presence of Cs close to Pt particles favours the CO release and inhibits the formation of C* species by CO dissociation at lower temperatures. Fig. 12 includes a schematic representation for this proposed reaction pathway. This is a highly important aspect to develop a stable catalyst for low-temperature RWGS.

4. Conclusions

Running the RWGS reaction at low-temperature represents a step ahead in gas-phase CO_2 conversion reactions. This process entails a big challenge which is the suppression of the competitive methanation process, and our study showcases that Cs-promoted Pt/TiO_2 is a promising catalyst to circumvent this challenge. Our *operando* analysis casts lights on the exceptional behaviour of Cs as a dopant which enables different mechanistic pathways when compared to the unpromoted system. More specifically, Pt/TiO_2 works under a redox mechanism where CO_2 dissociates to CO in the oxygen vacancies. Then, H_2 migrates by spill over recovering these oxygen vacancies so they are *in situ* generated and consumed circularly during the reaction. On the other hand, the Pt–Cs/TiO_2 mechanism allows two possible pathways: the (i) formyl/acyl pathway, where –CHO species are formed and, depending on the reaction conditions, evolve to CO gas or oxygenated compounds, and (ii) frustrated Lewis pair assisted CO_2 reduction route, in which FLPs induce the heterolytic dissociation of H_2 and the subsequent hydrogenation of CO_2 to CO. Our results demonstrate that Cs inhibits the formation of C* on Pt particles at low temperature, which is an important approach to design a low temperature catalyst for the RWGS reaction. The impact of Cs on the reaction pathway and ultimately on the activity and selectivity is mainly due to an electronic effect being an electropositive species that can donate electrons and create electronic rich sites to activate the reactants. However, beyond electronic promotion Cs is also a structural promoter enhancing Pt nanocluster dispersion leading to high performing RWGS materials.

All in all, this work charts a path to design highly effective multicomponent catalysts for low-temperature RWGS where Cs plays a crucial role as a promoter. Beyond materials chemistry, optimised catalysts for low-RWGS open a route for process engineering when it comes to integrating RWGS units within CO_2 utilization schemes saving capital and running costs, thus representing a tangible example for how advanced catalysts are essential for the transition towards a circular economy.

Author contributions

G. Torres-Sempere: conceptualisation, methodology, validation, formal analysis, investigation, writing – original draft. R. Blay: methodology, validation, formal analysis, investigation, visualisation. J. L. Santos: investigation, methodology. L. A. Luque: investigation. L. F. Bobadilla: methodology, formal analysis, resources, writing – original draft, writing – review & editing, visualisation, supervision. L. Pastor-Perez: resources, supervision, review. M. A. Centeno: investigation. W.·Y: Hernández: investigation. I. Yousef: investigation, methodology, validation, formal analysis. José Antonio Odriozola: formal analysis, resources, funding acquisition. Tomás R. Reina: conceptualisation, methodology, resources, writing – review & editing, supervision, project administration, funding acquisition.

Conflicts of interest

The authors declare no conflicts of interest.

Acknowledgements

The team at the University of Seville acknowledges financial support from the Spanish Ministry of Science through the projects NICER-BIOFUELS (ref: PLEC2021-008086), sponsored by MCIN/AEI/10.13039/501100011033 Next Generation Europe and SMART-FTS (ref: PID2021-126876OB-I00). Authors also acknowledge access to ALBA's facilities and support provided by ALBA's staff.

References

1 J. Hansen, M. Sato, R. Ruedy, K. Lo, D. W. Lea and M. Medina-Elizade, *Proc. Natl. Acad. Sci. U. S. A.*, 2006, **103**, 14288–14293.

Open Access Article. Published on 11 December 2023. Downloaded on 11/9/2025 9:25:01 AM.
This article is licensed under a Creative Commons Attribution 3.0 Unported Licence.

2 J. Ma, N. Sun, X. Zhang, N. Zhao, F. Xiao, W. Wei and Y. Sun, *Catal. Today*, 2009, **148**, 221–231.
3 M. Mikkelsen, M. Jørgensen and F. C. Krebs, *Energy Environ. Sci.*, 2010, **3**, 43–81.
4 L. Yang, L. Pastor-Pérez, S. Gu, A. Sepúlveda-Escribano and T. R. Reina, *Appl. Catal., B*, 2018, **232**, 464–471.
5 Y. A. Daza and J. N. Kuhn, *RSC Adv.*, 2016, **6**, 49675–49691.
6 L.-P. Merkouri, T. R. Reina and M. S. Duyar, *Nanoscale*, 2022, **14**, 12620–12637.
7 E. Portillo, J. Gandara-Loe, T. R. Reina and L. Pastor-Pérez, *Sci. Total Environ.*, 2023, **857**, 159394.
8 U. Guharoy, T. Ramirez Reina, S. Gu and Q. Cai, *J. Phys. Chem. C*, 2019, **123**, 22918–22931.
9 E. Le Saché, L. Pastor-Perez, B. J. Haycock, J. J. Villora-Picó, A. Sepulveda-Escribano and T. R. Reina, *ACS Sustain. Chem. Eng.*, 2020, **8**, 4614–4622.
10 H. Xu, Y. Li, X. Luo, Z. Xu and J. Ge, *Chem. Commun.*, 2017, **53**, 7953–7956.
11 Z. Zhao, M. Wang, P. Ma, Y. Zheng, J. Chen, H. Li, X. Zhang, K. Zheng, Q. Kuang and Z.-X. Xie, *Appl. Catal., B*, 2021, **291**, 120101.
12 X. Wang, H. Shi, J. H. Kwak and J. Szanyi, *ACS Catal.*, 2015, **5**, 6337–6349.
13 C. Wang, E. Guan, L. Wang, X. Chu, Z. Wu, J. Zhang, Z. Yang, Y. Jiang, L. Zhang and X. Meng, *J. Am. Chem. Soc.*, 2019, **141**, 8482–8488.
14 Y. Zhang, L. Liang, Z. Chen, J. Wen, W. Zhong, S. Zou, M. Fu, L. Chen and D. Ye, *Appl. Surf. Sci.*, 2020, **516**, 146035.
15 Q. Zhang, L. Pastor-Pérez, Q. Wang and T. R. Reina, *J. Energy Chem.*, 2022, **66**, 635–646.
16 Y. Tao, Y. Zhu, C. Liu, H. Yue, J. Ji, S. Yuan, W. Jiang and B. Liang, *J. Environ. Chem. Eng.*, 2018, **6**, 6761–6770.
17 S. S. Kim, H. H. Lee and S. C. Hong, *Appl. Catal., A*, 2012, **423**, 100–107.
18 M. Zhu, Q. Ge and X. Zhu, *Trans. Tianjin Univ.*, 2020, **26**, 172–187.
19 M. González-Castaño, B. Dorneanu and H. Arellano-García, *React. Chem. Eng.*, 2021, **6**, 954–976.
20 M. González-Castano, J. C. Navarro De Miguel, F. Sinha, S. Ghomsi Wabo, O. Klepel and H. Arellano-Garcia, *J. CO2 Util.*, 2021, **46**, 101493.
21 E. L. Fornero, D. L. Chiavassa, A. L. Bonivardi and M. A. Baltanás, *J. CO2 Util.*, 2017, **22**, 289–298.
22 A. Goguet, F. C. Meunier, D. Tibiletti, J. P. Breen and R. Burch, *J. Phys. Chem. B*, 2004, **108**, 20240–20246.
23 Z. Chen, L. Liang, H. Yuan, H. Liu, P. Wu, M. Fu, J. Wu, P. Chen, Y. Qiu, D. Ye and L. Chen, *Appl. Catal., B*, 2021, **298**, 120507.
24 S. S. Kim, H. H. Lee and S. C. Hong, *Appl. Catal., B*, 2012, **119–120**, 100–108.
25 G. Varvoutis, M. Lykaki, E. Papista, S. A. C. Carabineiro, A. C. Psarras, G. E. Marnellos and M. Konsolakis, *J. CO2 Util.*, 2021, **44**, 101408.
26 L. Yang, L. Pastor-Pérez, J. J. Villora-Pico, S. Gu, A. Sepúlveda-Escribano and T. R. Reina, *Appl. Catal., A*, 2020, **593**, 117442.
27 L. F. Bobadilla, J. L. Santos, S. Ivanova, J. A. Odriozola and A. Urakawa, *ACS Catal.*, 2018, **8**, 7455–7467.
28 W. Wang, S. Wang, X. Ma and J. Gong, *Chem. Soc. Rev.*, 2011, **40**, 3703–3727.
29 N. Ishito, K. Hara, K. Nakajima and A. Fukuoka, *J. Energy Chem.*, 2016, **25**, 306–310.
30 S. Challagulla, K. Tarafder, R. Ganesan and S. Roy, *Sci. Rep.*, 2017, **7**, 8783.
31 G. Leofanti, M. Padovan, G. Tozzola and B. Venturelli, *Catal. Today*, 1998, **41**, 207–219.
32 L. Pastor-Pérez, M. Shah, E. Le Saché and T. R. Reina, *Catalysts*, 2018, **8**, 608.
33 C. Zhang, G. Zhao, K. Liu, Y. Yang, H. Xiang and Y. Li, *J. Mol. Catal. A: Chem.*, 2010, **328**, 35–43.
34 B. Liang, H. Duan, X. Su, X. Chen, Y. Huang, X. Chen, J. J. Delgado and T. Zhang, *Catal. Today*, 2017, **281**, 319–326.
35 E. R. Silva, J. M. Silva, P. Massiani, F. R. Ribeiro and M. F. Ribeiro, *Catal. Today*, 2005, **107–108**, 792–799.
36 M. Primet, M. Mathieu, M. Primet, P. Pichat and M.-V. Mathieu, *J. Phys. Chem.*, 1971, **75**, 1216–1220.
37 L. Lan, H. Daly, Y. Jiao, Y. Yan, C. Hardacre and X. Fan, *Int. J. Hydrogen Energy*, 2021, **46**, 31054–31066.
38 A. Y. Stakheev, E. S. Shpiro, N. D. Zelinsky, N. I. Jaeger and G. Schulz-Eldoff, *Catal. Lett.*, 1995, **32**, 147–158.
39 S. Shen, X. Wang, Q. Ding, S. Jin, Z. Feng and C. Li, *Chin. J. Catal.*, 2014, **35**, 1900–1906.
40 F. Romero-Sarria, S. Garcia-Dali, S. Palma, E. M. Jimenez-Barrera, L. Oliviero, P. Bazin and J. A. Odriozola, *Surf. Sci.*, 2016, **648**, 84–91.
41 P. Panagiotopoulou and D. I. Kondarides, *J. Catal.*, 2009, **267**, 57–66.
42 P. Bazin, O. Saur, J. C. Lavalley, M. Daturi and G. Blanchard, *Phys. Chem. Chem. Phys.*, 2005, **7**, 187–194.
43 J. C. Calabrese, D. Lawrence, A. Cavalieri, P. Chini, G. Longoni and S. Martinengo, *J. Am. Chem. Soc.*, 1974, **96**(8), 2614–2616.
44 W. Li, J. Gan, Y. Liu, Y. Zou, S. Zhang and Y. Qu, *Angew. Chem., Int. Ed.*, 2023, **62**, e20235661.
45 J. C. Seo, G. Park, M. W. Arshad, C. Zhang, S. Kim and S. K. Kim, *J. CO2 Util.*, 2022, **66**, 102291.
46 K. K. Ghuman, L. B. Hoch, T. E. Wood, C. Mims, C. V. Singh and G. A. Ozin, *ACS Catal.*, 2016, **6**, 5764–5770.
47 K. K. Ghuman, T. E. Wood, L. B. Hoch, C. A. Mims, G. A. Ozin and C. V. Singh, *Phys. Chem. Chem. Phys.*, 2015, **17**, 14623–14635.
48 C. Liu, S. L. Nauert, M. A. Alsina, D. Wang, A. Grant, K. He, E. Weitz, M. Nolan, K. A. Gray and J. M. Notestein, *Appl. Catal., B*, 2019, **225**, 117754.
49 L. F. Bobadilla, A. Egaña, R. Castillo, F. Romero-Sarria, M. A. Centeno, O. Sanz, M. Montes and J. A. Odriozola, *Fuel*, 2022, **312**, 122964.
50 A. Jurado, Á. Morales-García, F. Viñes and F. Illas, *ACS Catal.*, 2022, **12**, 15658–15667.
51 L. F. Bobadilla, V. Garcilaso, M. A. Centeno and J. A. Odriozola, *ChemSusChem*, 2017, **10**, 1193–1201.
52 J. H. Bitter, K. Seshan and J. A. Lercher, *J. Catal.*, 1999, **183**, 336–343.
53 K. Hadjiivanov, *Appl. Surf. Sci.*, 1998, **135**, 331–338.

54 Y. Zhao, C. Li, X. Liu, F. Gu, H. Jiang, W. Shao, L. Zhang and Y. He, *Mater. Lett.*, 2007, **61**, 79–83.
55 L. Qin, G. Wang and Y. Tan, *Sci. Rep.*, 2018, **8**, 16198.
56 C. Zhang, J. Qi, Y. Li, Q. Han, W. Gao, Y. Wang and J. Dong, *Nanomaterials*, 2022, **12**, 1329.
57 R. Bower, C. P. T. McPolin, A. V. Krasavin, A. V. Zayats and P. K. Petrov, *Opt. Mater. Express*, 2022, **12**, 3471.
58 F. Zamboni, A. Makarevičiūtė and V. N. Popok, *Appl. Nano*, 2022, **3**, 102–111.
59 P. Makuła, M. Pacia and W. Macyk, *J. Phys. Chem. Lett.*, 2018, **9**, 6814–6817.

Open Access Article. Published on 11 December 2023. Downloaded on 11/9/2025 9:25:01 AM.
This article is licensed under a Creative Commons Attribution 3.0 Unported Licence.

 This journal is © The Royal Society of Chemistry 2024